



Tide-tsunami interaction in a highly energetic channel. A case study.

P. Winckler⁽¹⁾, I. Sepúlveda⁽²⁾, F. Aron^(3,4), M. Contreras-López⁽⁵⁾, P. L.-F. Liu^(6,7)

⁽¹⁾ Associate Professor. Escuela de Ingeniería Civil Oceánica, Universidad de Valparaíso. patricio.winckler@uv.cl

⁽²⁾ PhD student. School of Civil and Environmental Engineering, Cornell University. is328@cornell.edu

⁽³⁾ Postdoctoral Research Fellow. Departamento de Ingeniería Estructural y Geotécnica, Pontificia Universidad Católica de Chile. faron@ing.puc.cl

⁽⁴⁾ Visiting Scholar, Department of Geological Sciences, Stanford University.

⁽⁵⁾ Profesor Titular. Facultad de Ingeniería y Centro de Estudios Avanzados, Universidad de Playa Ancha. manuel.contreras@upla.cl

⁽⁶⁾ Distinguished Professor. Vice President (Research & Technology). National University of Singapore. dprllfp@nus.edu.sg

⁽⁷⁾ Class of 1912 Professor in Engineering, School of Civil and Environmental Engineering, Cornell University

Abstract

The present study is intended to improve the physical understanding of tsunami propagation in semi-confined water bodies where the interaction with tides plays a significant role. A case study in Canal Chacao, a highly energetic channel located at the norther extreme of Chilean Patagonia, is studied. The fundamental question addressed here is to understand the interactions when tides and tsunamis are linearly superposed and when they interact nonlinearly, thus enhancing or reducing the surface elevation and associated currents. To answer this question, we implemented a series of models based on the two-dimensional nonlinear shallow water equations to simulate the propagation of i) a tsunami with a constant tide corresponding to the mean sea level, ii) a tide and tsunami under the assumption that both can be linearly superimposed and iii) a tide and tsunami nonlinear interaction model. Results are analyzed in the narrowest section of Canal Chacao, where tidal currents may reach up to 6 m/s during spring tides. For this site, the maximum surface elevation during the simulation is larger in the nonlinear model, while the maximum current speeds (and derived quantities such as the drag forces or sediment transport potential) are obtained with the linear model. The nonlinear model is also better in computing the time of arrival of the first wave. These outcomes provide guidelines for the improvement of tsunami hazard assessments for the coastal communities located in fjords, channels and estuaries with similar characteristics.

Keywords: Tide, tsunami, nonlinear interaction, numerical modeling, Canal Chacao.



1. Introduction

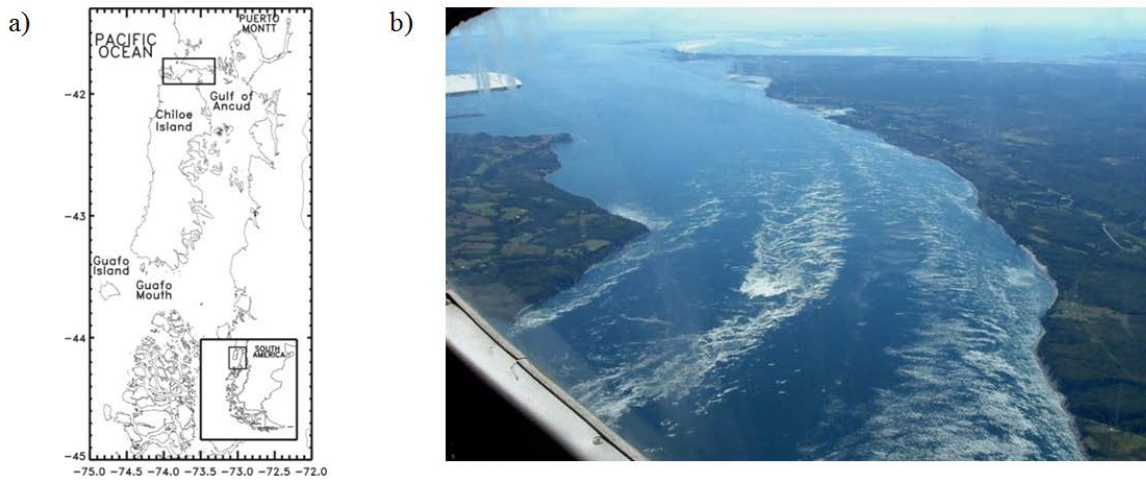
Tide-tsunami interaction can be assessed using different approaches with increasing levels of complexity depending on the scope of the study and local conditions of the site. The simplest is to compute the tsunami evolution with constant tide based on the assumption that the tidal currents are weak and the tide period is much longer than the tsunami. A more refined analysis can be achieved by a linear superposition of the tide and the tsunami, under the assumption that both oscillations are considered independent [1]. This approach is referred to as composite model hereafter. Recent studies, however, have found that composite models provide inaccurate results in shallow waters [2,3,4,5,6,7]. The most complete approach can be achieved by numerically computing the tsunami and the tide together. This approach -referred to as full model- is appropriate for regions where nonlinear effects may be important due to very strong tides or relatively shallow bathymetries. Based on numerical experiments, [3,5] found that i) tidal elevations influence the speed and magnitude of tsunami waves in shallow regions, ii) elevations from full and composite models differ significantly and iii) tsunami-tide interaction depends on tidal amplitude and phase. The major cause of this interaction is tidally induced changes in the ocean depth and currents altering the conditions of tsunami propagation, amplification and dissipation.

The present work is intended to improve the physical understanding of tide-tsunami interaction in Canal Chacao, a highly energetic channel which connects the Pacific Ocean with the Chilean Inland Sea, CIS (Figure 1a). This channel is dominated by tidal currents caused by differences in tidal range and phase between its extremes. Canal Chacao is approximately 26 km long and connects Coronados Gulf in the open ocean with the Ancud Gulf in the CIS. Its narrowest section, the 2.2 km wide channel exhibits an isolated pinnacle, Roca Remolinos, which separates the stream in two smaller waterways [8]. Maximum speeds may reach peaks of about 6 m/s during spring tide in Roca Remolinos (Figure 1b). The channel is sited in a region prone to large earthquakes and tsunamis [9]. To understand the consequences of the modeling approach, we implemented a two-dimensional shallow water model to solve the propagation of i) a tsunami with a constant tide corresponding to the mean sea level, ii) a composite tide-tsunami model under the assumption that both can be linearly superimposed and iii) a full tide-tsunami nonlinear interaction model. A tide model covering a lunar cycle of 28 days was also implemented to cover extreme events during spring and neap tides. Results are analyzed in Roca Remolinos. Eleven tidal constituents are used for the tide model, while no meteorological forcings are considered.

2. Tide model

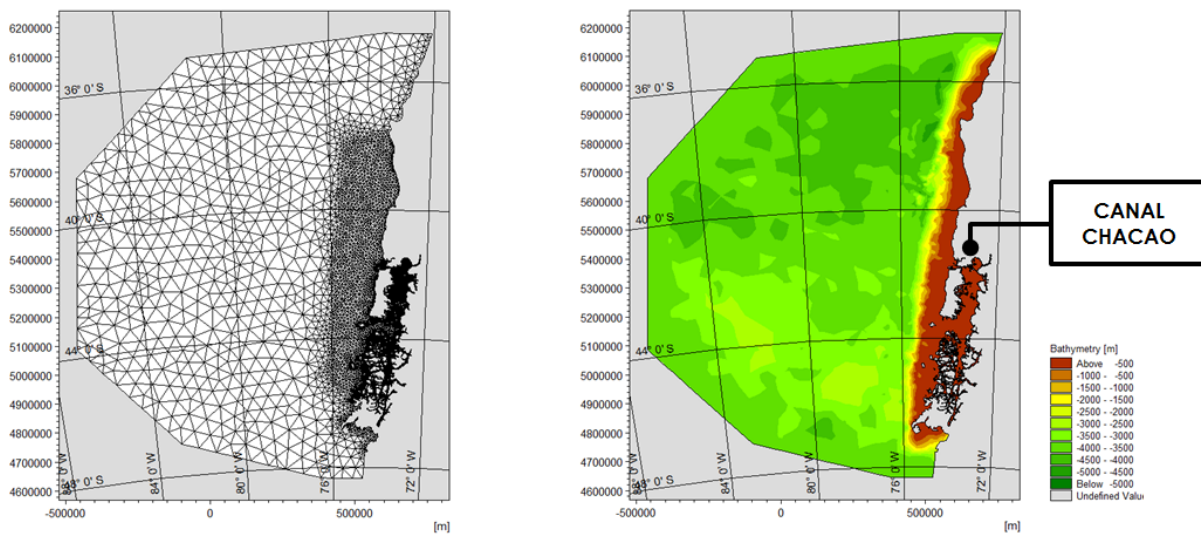
Tidal effects were implemented using the concept of the equilibrium tide via additional terms in the momentum equations and boundary conditions [10]. The tide model was developed using a two-dimensional model on a flexible finite volume mesh [11]. The model resolves the nonlinear shallow-water equations (NSWE) resulting from depth averaging the three-dimensional incompressible Reynolds averaged Navier-Stokes equations, under the assumption of hydrostatic pressure. The bottom stress was modeled with a quadratic friction law with a constant Manning's value of $n = 0.034 \text{ s/m}^{1/3}$ due to lack of site specific data for bottom roughness. In the offshore boundaries, a value of $n = 0.2 \text{ s/m}^{1/3}$ was used to damp instabilities. An eddy viscosity of $A = 0.06 \text{ m}^2/\text{s}$ in the domain and $A = 0.2 \text{ m}^2/\text{s}$ at the offshore boundaries to control spurious instabilities during the warming up phase of the tidal simulation was used. It should be noted that the tidal currents were found to be insensitive to a wide range of values of the Manning coefficient and eddy viscosity. A flooding and drying scheme was used even though the analysis of run-ups was not part of the scope of the study.

Figure 1: a) The Chilean Inland Sea and Canal Chacao in a box. b) Aerial view of the narrowest section of Canal Chacao during ebb tide. The Pacific Ocean is observed in the background while Roca Remolinos, characterized by a turbulent wake, is at the center of the image (courtesy of Horacio Parragué).



The digital elevation model (DEM) was built using a cell-centered finite volume method in an unstructured grid of 57.741 triangular elements, with relatively large elements in the deep ocean and smaller ones in the CIS (Figure 2). The DEM penetrates roughly 1300 km in the Pacific Ocean and extends 1300 km in the North-South direction. The DEM was built from the Etopo 1 arc-minute global relief in the open ocean [12], 14 nautical charts [13] in coastal areas within the CIS and a 0.5 m resolution bathymetry in the vicinity of Roca Remolinos, where the analysis is focused. The resolution varied from of $\sim 1.600 \text{ km}^2$ in the deep ocean, successively increasing to $\sim 2.500 \text{ m}^2$ in the narrowest section of the channel. The grid size was refined locally in the rupture zone of the 1960 Chile earthquake to guarantee that the initial tsunami wavelength was resolved by at least 20 grid points. A time step of 0.5 s was chosen to ensure numerical stability of the model. The extent and resolution of the DEM is a significant improvement compared to earlier studies [14,15,16,17,18].

Figure 2: Left panel shows the numerical grid used in the DEM and right panel depicts the water depth.

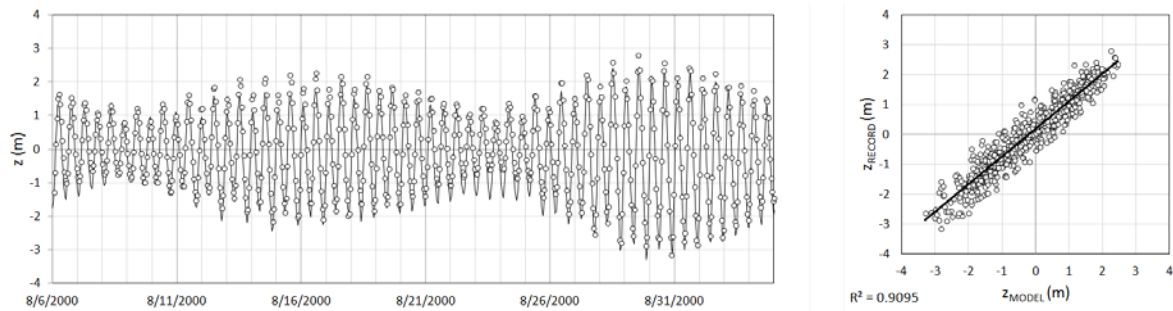


Tides were ramped for 2 days until dynamic equilibrium was reached (i.e. when the tide signal becomes independent of the initial condition). The model was calibrated with a field survey covering between August 6th



and September 5th 2000. Calibration consisted in i) defining the minimum amount of tidal constituents to adequately reproduce the records in tidal gauges and ADCP's within Canal Chacao, ii) evaluating the frictional effects for a range of values of the Manning coefficient and iii) tuning the eddy viscosity to account for momentum diffusion. The sensitivity of results under a wide range of values for the Manning and eddy viscosity coefficients was low while the number of tidal constituents was determinant in achieving good results. Eleven major diurnal constituents (K1, O1, P1 and Q1), semidiurnal tidal constituents (M2, S2, N2 and K2) and other constituents (Mf, Mm, Ssa) varying in space and time were specified within the domain using a Global Ocean Tides Model [19]. Surface elevations from the model were compared with tide gauges within Canal Chacao showing correlations of $R^2 = 90-94\%$. As an example, Figure 3 shows the model-to-data comparisons of surface elevation in Eje 1. Depth-averaged velocities showed correlations between $R^2 = 57-72\%$

Figure 3: Calibration of surface elevation in Eje 1. Left: time series of the model in continuous line and record in circles. Right: correlation between measured (z_{RECORD}) and modelled values (z_{MODEL}).



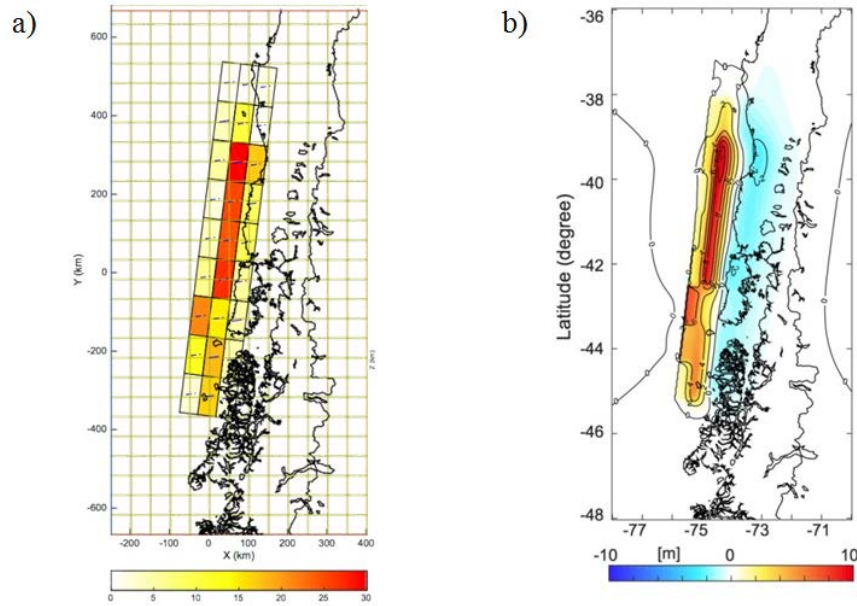
3. Rupture model

The vertical component of the seafloor deformation was computed herein using the standard dislocation theory [20] and the slip distribution proposed in [21]. The model runs in an elastic half-space medium limited by the inclined submarine continental talus. We corrected for the slope of the oceanic talus following the methodology proposed by [22], so the seafloor coincides with the free surface of the semi-infinite half-space used to estimate earthquake-induced deformation in the elastic medium. Along the rupture length, the trench (intersection between the two tectonic plates) lies at approximately 3 km depth and the talus has a slope of about 2° down to the trench. The coordinate system was translated and rotated so the trench constitutes a new y' -axis of the rotated

system. Accounting for a more realistic geometry of the fault and medium, this correction permits precise estimations of the vertical displacements of the sea bottom. For all the computations, an elasticity modulus of $E = 80$ GPa, a shear modulus of $G = 32$ GPa and Poisson's ratio of $\nu = 0.25$ were used as average crustal values in the rupture area [23]. Figure 4b shows a positive coseismic uplift of the sea bottom, in a pseudo-ellipsoidal pattern, and a smaller subsidence inland from the coastline. The seafloor subsidence is of approximately -1.7 m in Canal Chacao.

For tsunami modelling, the initial surface elevation is assumed to be equivalent to the seafloor vertical deformation. This assumption is based on the fact that the time scale of the rupture is significantly larger than the time scale of the evolution of the tsunami. The vertical deformation was also included as a change of bathymetry (subsidence and/or uplift) at the moment of the earthquake.

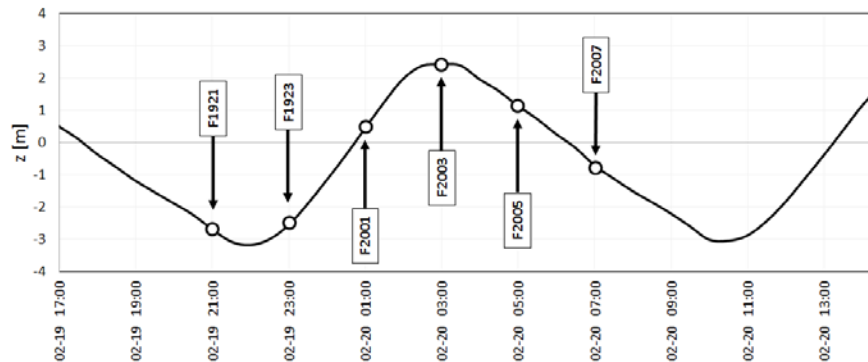
Figure 4: a) Slip distributions proposed by Fujii & Satake (2013). b) Vertical displacement of the seafloor, obtained using Okada (1992) model.



4. Tide-tsunami models

Three types of models were implemented to solve the propagation of i) a 1960-type tsunami with a constant tide equivalent to the mean sea level (tsunami model), ii) the tide and a 1960-type tsunami under the assumption that both can be linearly superimposed (composite model) and iii) a 1960-type tsunami under the assumption that it interact nonlinearly with the tide (full model). The tsunami model does not include tidal variations in space and time. In the composite and full models, however, the hydrodynamic patterns depend on the tidal phase occurring between the earthquake until the tsunami arrival to Roca Remolinos, and its spatial variation within the domain. The impact in the tidal phase is studied by means of 6 cases where the earthquake was triggered every 2 hours along the tidal cycle of 12.42 hours, so as to cover all the possible combinations (Figure 5). The tidal cycle corresponds to a spring tide of high amplitude, where the nonlinear interactions are expected to be enhanced due to the high tidal velocities. Results are analyzed in Roca Remolinos, at the narrowest section of the channel, where nonlinear interactions are also presumed to be relevant. To assure that the model is simulating the maximum tsunami heights and currents, 20 hours were simulated. Results, however, are shown during the first 3.5 hours of simulation since the tsunami signal is significantly attenuated afterwards.

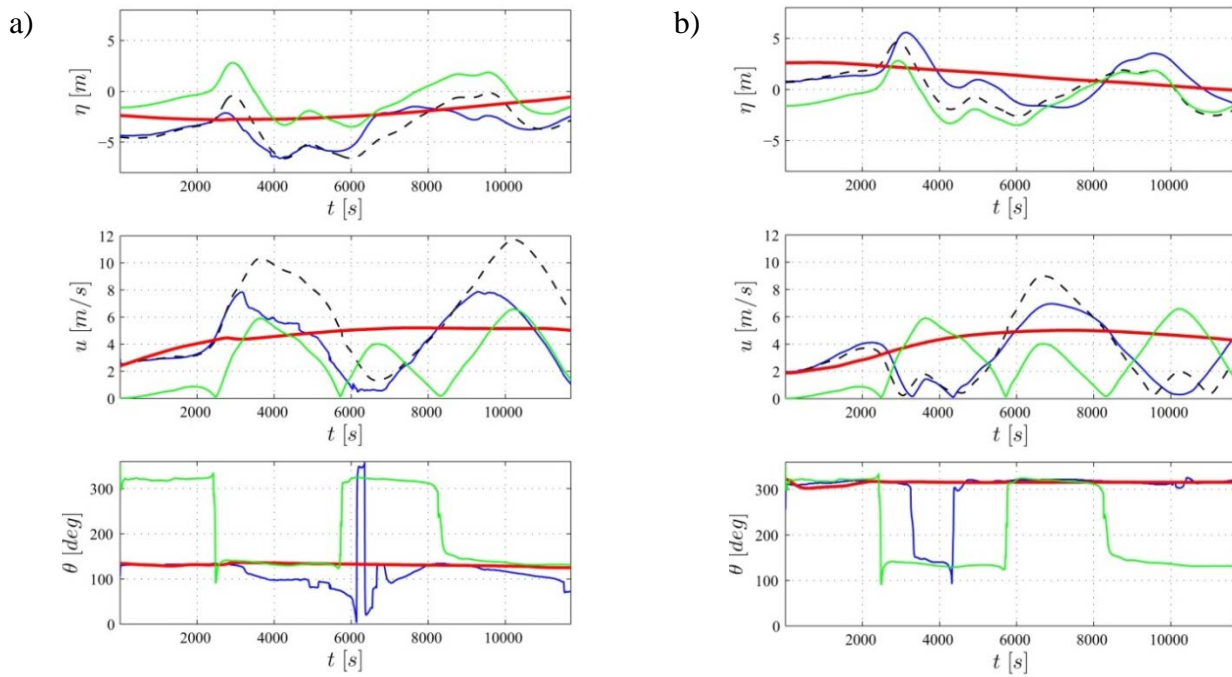
Figure 5: Nomenclature used for the composite and full tide-tsunami models.





Time series of elevation, current speed and direction in Roca Remolinos are shown in Figure 6 for the tide, tsunami, composite and full models in two cases (F1921, F2003). For a better comparison among cases, we establish $t = 0$ s as the time were the earthquake is triggered. In our reference system, a flood tide corresponds to a flow running towards the ESE ($\theta = 110^\circ$ - 130°) whereas an ebb tide flows to the WNW ($\theta = 300^\circ$ - 320°). Figure 7 and Figure 8 depict the results for amplitude and current speed for all the cases included in Figure 5. Note that the tsunami model initiates with negative amplitude as a consequence of a 1.7 m subsidence of the sea bottom caused by the earthquake. For the composite and full models, the initial amplitude considers both the coseismic deformation and the tide level. The resulting hydrodynamic patterns differ significantly, being the composite and full models strongly dependent on the tide signal. Depending on the relative magnitudes and phases astronomical tides, the tsunami may experience a significantly different background current. Naturally, the shape of the time series of surface amplitude for the composite model resembles the tsunami model as it stems from the sum of the latter with the tide, which is a smooth signal. In the full model, in contrast, complex small-scale fluctuations ride on top of the larger scales.

Figure 6: Surface elevation (upper panels), current speed (center panels) and directions (lower panels) for tide (red), tsunami (green), composite (black) and full (blue) models F1921 (a) and F2003 (b).



The maximum amplitude and velocity during the tsunami attack are valuable parameters for the design of maritime and coastal works. Figure 7 summarizes the results of the amplitude (η_{max}) throughout the computation obtained for all the models. For comparison, the following parameter is introduced:

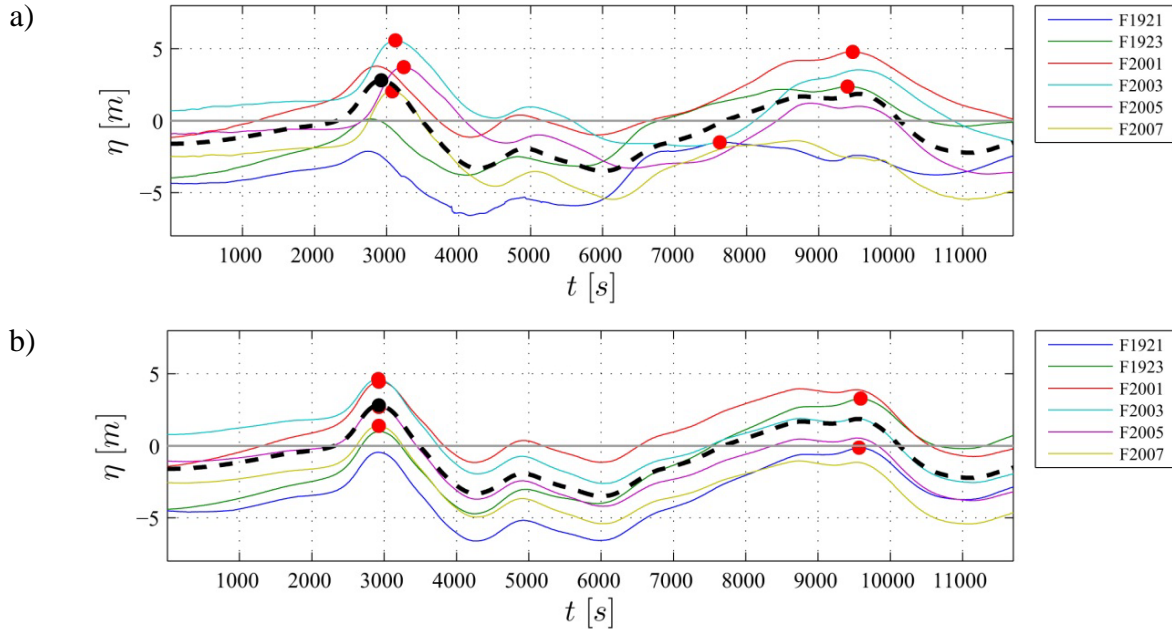
$$\Delta\eta = \eta_{(ti-tsu)}^{max} - \eta_{(tsu)}^{max} \quad (1)$$

where $\eta_{(ti-tsu)}^{max}$ corresponds to the maximum amplitude throughout the computation for the composite and full models and $\eta_{(tsu)}^{max}$ is the maximum amplitude obtained with the tsunami model, considered as reference since it represents the customary approach for engineering purposes. As expected, relatively high amplitudes occur during high tides (cases F2001, F2003 and F2005) while low values are observed in low tides (cases F1921, F1923 and F2007). Maximum amplitudes obtained among models differ significantly, being the full model the one providing higher (F2003) and lower values (F1921). The differences with respect to the tsunami model are comparable to the typical values of the amplitude ($\Delta\eta = -2.77$ m for case F2003 and $\Delta\eta = -4.30$ m for case F1921, where $\eta_{(tsu)}^{max} = 2.80$ m). Note that the maximum amplitude is not always related to the leading wave (e.g.



cases F1921, F1923 and F2001 in the composite model and F1921 and F1923 in full mode) mainly due to higher tides during the attack of the second wave. Higher amplitudes occurring after the leading wave impact have been observed in previous events due to edge waves travelling along the continental shelf [24] or a combination of high tide and tsunami.

Figure 7: Amplitudes obtained with the a) composite and b) full models. The tsunami model is depicted in segmented lines. Red dots indicate the maximum values which values are included in the table, together with the differences with respect to the tsunami model. The table below provides relevant values.



Case	Tide		Full		Composite	
	Direction	$\eta_{(mar)}$	η_{max}	$\Delta\eta_{max}$	η_{max}	$\Delta\eta_{max}$
			[m]	[m]	[m]	[m]
F1921	Flood	-1,96	-1,50	-4,30	-0,14	-2,94
F1923	Flood	-1,72	2,37	-0,43	3,27	0,47
F2001	Transition	1,07	4,79	1,99	4,46	1,66
F2003	Ebb	3,03	5,57	2,77	4,62	1,82
F2005	Ebb	1,43	3,72	0,92	2,70	-0,10
F2007	Transition	-0,27	2,05	-0,75	1,39	-1,41
Tsunami	-	0,00	2,80	-	2,80	-

Figure 9 summarizes the results for the maximum velocity (u_{max}) obtained for all models. The parameter

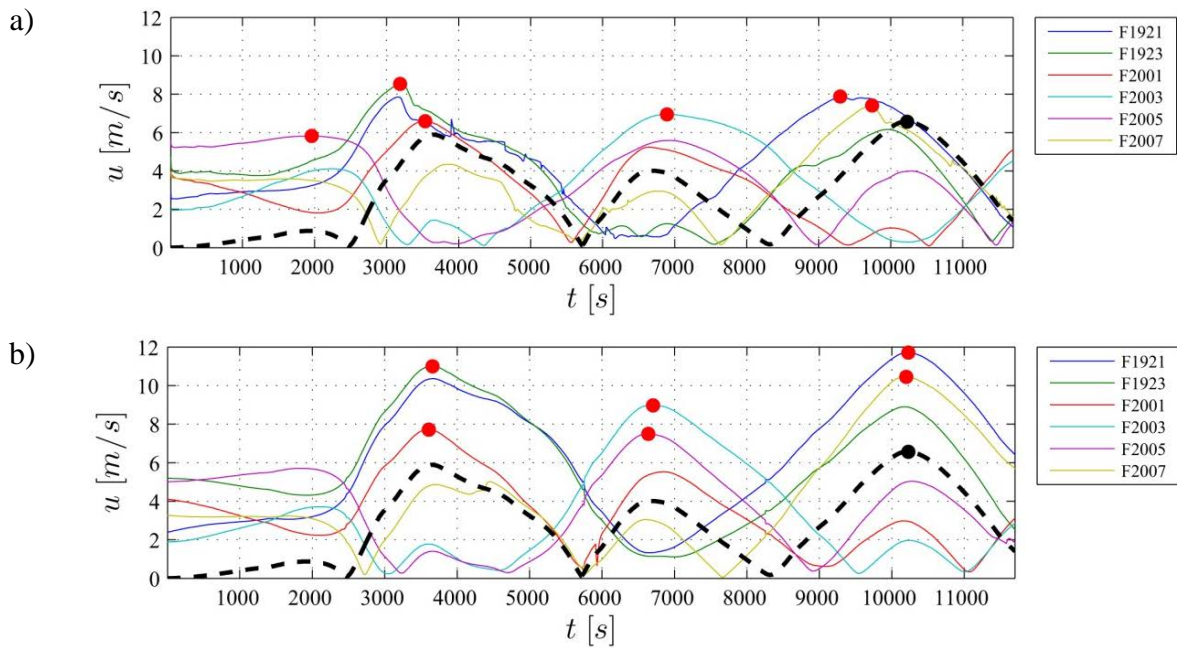
$$\Delta u = u_{(ti-tsu)}^{max} - u_{(tsu)}^{max} \quad (2)$$

is introduced, where $u_{(ti-tsu)}^{max}$ is the maximum current speed throughout the simulation for the composite and full models and $u_{(tsu)}^{max}$ is the maximum obtained with the tsunami model. With the exception of case 2005 -which corresponds to an ebb tide during high tides- maximum current speeds obtained with the composite and full models exceed those for the tsunami model (Figure 8a). The full model, however, provides slightly larger values



than the latter, while the composite model gives significantly large ones, e.g. $\Delta u = 5.13$ m/s for the composite and $\Delta u = 1.95$ m/s for the full model during the flood phase in low tide (F1923). Differences in maximum velocities have profound consequences in drag velocities (proportional to the square of the velocity) which may in turn determine the sediment transport potential and hydrodynamic forces on structures. As an example, for maximum velocities of 8.53 m/s for the full and 11.71 m/s for the composite models, drag forces are 1.68 and 3.17 times those obtained with 6.58 m/s computed with the tsunami model.

Figure 8: Velocities obtained with the a) composite and b) full models. The tsunami model is depicted in segmented lines. Red dots indicate the maximum values which values are included in the table, together with the differences with respect to the tsunami model. The table below provides relevant values.



Case	Tide		Full		Composite	
	Direction	$\bar{\eta}(\text{max})$	u_{max}	Δu_{max}	u_{max}	Δu_{max}
			[m]	[m]	[m]	[m]
F1921	Flood	-1,96	7,87	1,29	11,71	5,13
F1923	Flood	-1,72	8,53	1,95	11,01	4,43
F2001	Transition	1,07	6,59	0,01	7,73	1,15
F2003	Ebb	3,03	6,96	0,38	8,98	2,40
F2005	Ebb	1,43	5,82	-0,76	7,50	0,92
F2007	Transition	-0,27	7,42	0,84	10,45	3,87
Tsunami	-	0,00	6,58	-	6,58	-



5. Conclusion

The hydrodynamic patterns associated to the impact of a large 1960-type tsunami on a highly energetic channel have been analyzed by means of three models with increasing level of complexity: a tsunami model with quiescent tide, a composite model based on linear superposition of tide and tsunami and a full model accounting for nonlinear interactions between these long waves. We find that the hydrodynamic patterns in Canal Chacao differ significantly among models, being the composite and full models very sensitive to the tidal phase at which the tsunami is triggered. Indeed, some wave features obtained at Roca Remolinos with the full and composite models do not emerge in the pure tsunami simulations.

The characteristics of the incident tsunami are significantly modified when entering Canal Chacao as a consequence of the nonlinear shallow water dynamics. The amplification or reduction of the amplitude and phase speed is controlled by the tidal phase. The amplitudes obtained with both the composite and full models are mostly dependent on i) the total depth changing in time and space as the tsunami rides the tide and ii) the direction and magnitude of the tidal current. Maximum amplitudes throughout the simulation are larger for the full model and are not necessarily associated to the leading wave, due to (in some cases) the higher tide coinciding with secondary waves. For the maximum velocities throughout the simulation, the composite model provides larger values, which may in turn have consequences in derived quantities such as drag forces or sediment transport potential. Finally, the full model better captures the anticipation (or delay) of the leading wave as a consequence of the nonlinear interaction between the flood (ebb) tide and the tsunami. These results, however, cannot be extrapolated to other cases since the interactions between tides and tsunami depend upon the bathymetry and configuration of the coastline, the relative strength (i.e. amplitude and velocity) of the tide with respect to the tsunami and the rupture model. An ongoing step forward is to analyze simplified geometries to isolate the impact of each of these effects in the hydrodynamics.

Currently, tsunami risk assessments seldom include nonlinear interactions between tide and tsunami. However, in semiconfined water bodies with high tidal ranges where large tsunamis may occur, these interactions should be taken into account to gain accuracy on the results. The methodology presented herein may be expanded to define, from a more general perspective and for other configurations, under which conditions tides and tsunamis can be linearly superposed and in which conditions they interact nonlinearly. The outcomes of our investigation are essential for improving structural designs and tsunami hazard assessments for the coastal communities located in the area.

Acknowledgements

The authors would like to thank CONICYT (Chile) through its grant FONDECYT 11150003 entitled “Assessment of tide-tsunami interaction in fjords, channels and estuaries”. P. Winckler and I. Sepúlveda thank Fulbright and CONICYT for financial assistance in the form of studentships. The authors also acknowledge DHI for the sponsored MIKE academic licenses and SHOA and GEBCO for the digital bathymetric data used in the model. We thank F. Landeta for the interpretation of field data.

References

- [1] Bernard, E., Robinson, A. (Eds.) (2009). *The Sea, vol. 15, Tsunamis*. Harvard University Press, Cambridge, MA, 450 pp.
- [2] Kowalik, Z. and Proshutinsky, A. (2010). Tsunami–tide interactions: A Cook Inlet case study. *Continental Shelf Research* **30**, 633–642.
- [3] Kowalik, Z.; Proshutinsky, T. and Proshutinsky, A. (2006). Tide-tsunami interactions. *Sci. Tsunami Hazards*. 24 (4), 242–256.



- [4] Zhang, Y.J., Witter, R.C., Priest, G.R. (2011). Tsunami–tide interaction in 1964 Prince William Sound tsunami. *Ocean Modelling*. **40**: 246–259.
- [5] Tolikova, E. (2013). Tide-Tsunami Interaction in Columbia River, as Implied by Historical Data and Numerical Simulations. *Pure Appl. Geophys.* **170**(6), 1115–1126, doi: 10.1007/s00024-012-0518-0.
- [6] Shimoyama, T., Lee, H.S. (2014). Tsunami-tide interaction in the Seto inland sea, Japan. *International Conference on Coastal Engineering ICCE 2014*, Seoul, Korea.
- [7] Androsov, A., Behrens, J. & Danilov, S. (2011). Tsunami Modelling with Unstructured Grids. Interaction between Tides and Tsunami Waves, in: Krause, E. et al. (Eds.): *Computational Sci. & High Performance Computing. IV, NFM115*, pp. 191–206.
- [8] Cáceres, M., Valle-Levinson, A., Atkinson, L. (2003). Observations of cross-channel structure of flow in an energetic tidal channel. *Journal of Geophysical Research*, 108, No. C4, 3114, doi:10.1029/2001JC000968.
- [9] Cisternas, M., Atwater, B.F., Torrejón, F., Sawai, Y., Machuca, G., Lagos, M., Eipert, A., Youlton, C., Salgado, I., Kamataki, T., Shishikura, M., Rajendran, C.P., Malik, C.P., Rizal, Y., Husni, M. (2005). Predecessors of the giant 1960 Chile earthquake. *Nature*, **437**(7057): 404–407.
- [10] Pugh, D., Woodworth, P. (2014). *Sea-level science: understanding tides, surges, tsunamis and mean sea-level changes*. Cambridge University Press.
- [11] DHI (2011). *Mike 21 & Mike 3 Flow Model FM. Hydrodynamic and Transport Module*. Scientific documentation.
- [12] Amante, C. & Eakins, B.W. (2009). ETOPO1 1 arc-minute global relief model: Procedures, data sources and analysis, NOAA Technical Memorandum NESDIS NGDC-24, National Geophysical Data Center, U.S. Department of Commerce, Boulder, Colorado, 19 pp. <http://www.ngdc.noaa.gov/mgg/global/global.html> (accessed 26.03.2016).
- [13] SHOA (2009). *Atlas Hidrográfico de la Armada de Chile*, 7a Edición. Pub. 3042.
- [14] Warren, R.; Larsen, J. & Svendsen, H. (2007). *Chacao Channel, An Extreme Application of MIKE 21*. COWI Consulting Engineers and Planners AS, Lyngby, Denmark.
- [15] Campuzano, F. J., & Marín Briano, V. (2008). Un modelo hidrodinámico-barotrópico para los fiordos australes de Chile entre los 41° S y los 46° S. *Cienc. Tecnol. Mar*, **31** (2): 125-136.
- [16] Aiken, C.M. (2008). Barotropic tides of the Chilean Inland Sea and their sensitivity to basin geometry. *Journal of Geophysical Research*. **113**, C08024.
- [17] Sepúlveda, I., Winckler, P. and Cáceres, M. (2012). Hydrodynamic modeling of tidal currents and power extraction in Chacao Channel, Chile. *4th Annual Marine Renewable Energy Technical Conference*. University of Massachusetts Dartmouth. United States.
- [18] Lindeen, N. (2013). *Hydrodynamic modelling of tidal currents at Chacao Channel for a preliminary energy resource assessment*. Master of Science in Engineering. Pontificia Universidad Católica De Chile.
- [19] Andersen, O., (1995). Global ocean tides from ERS 1 and TOPEX/POSEIDON altimetry. *Journal of Geophysical Research*. **100**, C12, p. 25249-25260.
- [20] Okada, Y. (1992), Internal deformation due to shear and tensile faults in a half-space, *Bull. Seismol. Soc. Am.*, **82**(2), 1018-1040.
- [21] Fujii, Y., and Satake, K. (2013), Slip Distribution and Seismic Moment of the 2010 and 1960 Chilean Earthquakes Inferred from Tsunami Waveforms and Coastal Geodetic Data, *Pure Appl. Geophys.*, 170(9-10), 1493-1509, doi:10.1007/s00024-012-0524-2.
- [22] Flück, P., R. D. Hyndman, and K. Wang (1997), Three-dimensional dislocation model for great earthquakes of the Cascadia subduction zone, *Journal of Geophysical Research*, **102**(B9), 20539–20550.
- [23] Turcotte, D.L., Schubert, G. (2002). *Geodynamics*, 2nd Ed. Cambridge University Press, Cambridge, New York.
- [24] Catalán, P., Aránguiz, R., González, G., Tomita, T., Cienfuegos, R., González, J., Shrivastava M., Kumagai K., Mokrani C., Cortés P. & Gubler, A. (2015). The 1 April 2014 Pisagua tsunami: Observations and modeling. *Geophys. Res. Lett.*, 42.